JGR Oceans

RESEARCH ARTICLE
10.1029/2019JC015696

Response of the Pacific Sector of the Southern Ocean to Wind Stress Variability From 1995 to 2017

M. Menna[1], Y. Cotroneo[2,3], P. Falco[2,3], E. Zambianchi[2,3,4], R. Di Lemma[2], P.-M. Poulain[1], G. Fusco[2,3], and G. Budillon[2,3]

[1]National Institute of Oceanography and Applied Geophysics, Sgonico, Italy, [2]Department of Science and Technology, University of Naples "Parthenope", Naples, Italy, [3]CoNISMa, Consorzio Nazionale Interuniversitario per le Scienze del Mare, Rome, Italy, [4]CNR-ISMAR, Rome, Italy

Key Points:
- In situ data describe the interannual and decadal variability of the Antarctic Circumpolar Current in the Southern Pacific Ocean
- The interannual variability of the eddy field and of the eddy heat fluxes is related to the zonal wind stress field
- The meridional eddy heat fluxes show a larger variability on interannual than on decadal scales

Correspondence to:
M. Menna,
mmenna@inogs.it

Citation:
Menna, M., Cotroneo, Y., Falco, P., Zambianchi, E., Di Lemma, R., Poulain, P.-M., et al. (2020). Response of the Pacific Sector of the Southern Ocean to wind stress variability from 1995 to 2017. *Journal of Geophysical Research: Oceans*, *125*, e2019JC015696. https://doi.org/10.1029/2019JC015696

Received 25 SEP 2019
Accepted 11 OCT 2020
Accepted article online 15 OCT 2020

Abstract Drifter, satellite, expendable bathythermograph (XBT), and Argo float data are used to study the response of the Pacific Sector of the Southern Ocean (PSSO) to the wind stress field in the period 1995–2017, in terms of eddy field, water mass transport, and heat fluxes at large and regional scales. Increasing wind stress over the PSSO in those two decades led to a growth of the Eddy Kinetic Energy (EKE) in the region of the Antarctic Circumpolar Current (ACC). Increases of the EKE occur with delays of 1–4 years with respect to peaks in the zonal component of the wind stress. The persistent ACC meander located south of New Zealand (between 150°E and 180°W and 50°S to 66°S) responds to the interannual wind variations earlier than the entire ACC branch in the PSSO. In the same area, an estimate of the ACC transport based on in situ data shows interannual variability but no significant decadal trend over the study period. The effects of the EKE variability on the meridional eddy heat fluxes are significant on interannual scales. The strengthening of the EKE field leads to a local increase in the poleward meridional eddy heat fluxes in the PSSO, especially in the ACC band. The weakening of the EKE field defines an area of equatorward meridional eddy heat fluxes in the middle of the PSSO (south of 40°S, between 130°W and 160°W) and prevalent poleward fluxes in the further western and eastern regions.

1. Introduction

One of the most important climate changes in the Southern Hemisphere over the last decades has been the persistence of the Southern Annular Mode (SAM) in a positive state (e.g., Rintoul, 2018; Rintoul et al., 2018) that corresponds to an increase of the wind stress (Hande et al., 2012). Winds over the SO have strengthened since the 1950s (Patara et al., 2016) with positive trends of the wind stress, estimated both by in situ observations (Hande et al., 2012) and by atmospheric reanalysis products (National Centers for Environmental Prediction [NCEP-1] and European Centre for Medium-Range Weather Forecasts [ECMWF] Era-Interim reanalysis), range between 0.00023 and 0.00067 N m^{-2} $year^{-1}$ (Lin et al., 2018).

The Southern Ocean (SO) is characterized by high levels of Eddy Kinetic Energy (EKE) associated with the instabilities of the Antarctic Circumpolar Current (ACC) (Falco & Zambianchi, 2011; Naveira Garabato et al., 2011; Phillips & Rintoul, 2000; Sheen et al., 2014; Wunsch & Stammer, 1995). The eddy field has a complex interaction with wind stress fluctuations in the SO. According to linear theory, if the wind stress increases, the ACC volume transport rises linearly but the eddy field remains almost constant. In the last decades, many studies (e.g., Hogg et al., 2008, 2015; Jochum & Eden, 2015; Langlais et al., 2015; Meredith & Hogg, 2006; Patara et al., 2016; Rintoul & Naveira Garabato, 2013) have demonstrated that an increase in the wind stress drives an increase of the Available Potential Energy (APE) due to the augmented tilt of the isopycnals by the higher northward Ekman transport. However, once the APE saturates (the isopycnals cannot increase their tilt indefinitely), any additional APE is released through baroclinic instability. At that point, further strengthening of the wind stress field would induce changes primarily in the eddy field intensity, with relatively little change in the ACC volume transport because eddies act to flatten the isopycnals to keep the transport constant. This effect is known as "eddy saturation" (Straub, 1993), and its implications in SO dynamics depend on the interplay between wind stress, stratification, and topography flow interactions.

The response of the SO to wind stress changes has a stronger fingerprint in the Indian and Pacific Sectors than in the Atlantic sector (e.g., Hogg et al., 2015). The Pacific Sector of the SO (Figure 1—PSSO

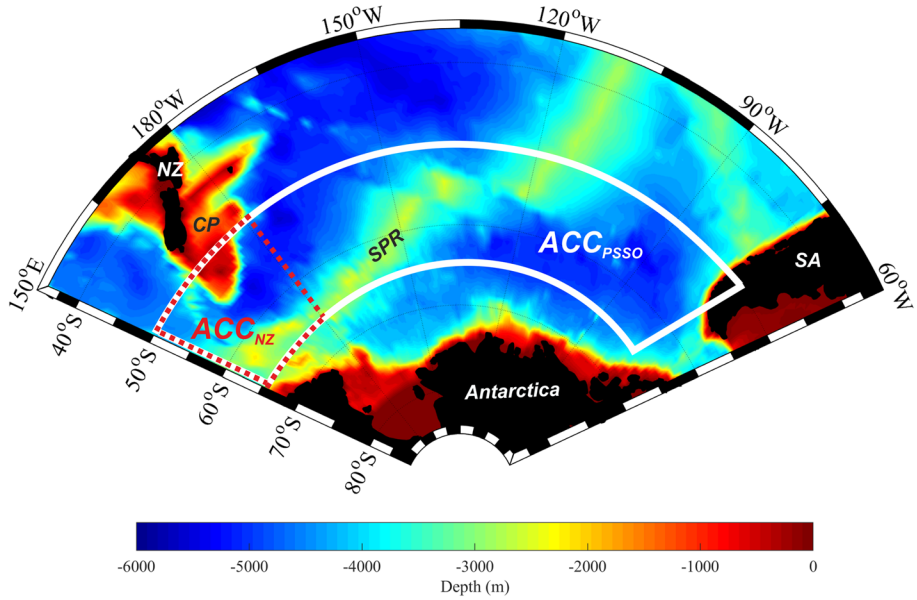

Figure 1. Geography and bathymetry of the PSSO. The white solid and the red dotted areas denote the ACC_{PSSO} and ACC_{NZ} sectors, respectively. Main geographical references are indicated as follows: New Zealand (NZ), Campbell Plateau (CP), South Pacific Ridge (SPR), and South America (SA).

hereafter) is characterized by the highest trend of wind stress and by a positive feedback between wind stress and the EKE field (Patara et al., 2016). Meredith and Hogg (2006) found a 2- to 3-year time lag between the wind and the EKE peaks in the SO with the highest EKE in the PSSO. The authors identified this lag as the time required for baroclinic eddies to extract, via baroclinic instability, APE created by wind-driven isopycnal tilting. Hogg et al. (2015) pointed out that the EKE response to enhanced wind stress occurs on time scales shorter than 5 years. Thompson and Naveira Garabato (2014) suggested the "flexing" of standing ACC meanders as an alternative mechanism for locally reducing the sensitivity of the ACC's baroclinicity to changes in forcing. Morrow et al. (2010) pointed out the role played by the El Niño–Southern Oscillation (ENSO) in enhancing or weakening the EKE field. An additional contribution to the SO dynamics is represented by its intrinsic variability (e.g., Wilson et al., 2015), related to the highly nonlinear oceanic mechanism internal to the ocean system (Sgubin et al., 2014).

The increase of the SO wind speed over the last decades and its relationship with the increase of the eddy field might influence the poleward heat fluxes across the ACC (e.g., Abernathey & Cessi, 2014; Hogg et al., 2008). The eddy field controls the oceanic poleward heat flux through the Eddy Heat Flux (EHF) (Foppert et al., 2017; Rintoul et al., 2001; Trani et al., 2011). The contribution of the transient processes associated with the horizontal circulation (eddies and seasonal/interannual variability of the ACC) is approximately one third of the total meridional heat fluxes due to the time mean horizontal circulation (Volkov et al., 2010).

In this work, we exploit an extensive data set of observations gathered in the PSSO, consisting of a 20-year repeated track expendable bathythermograph (XBT) section, along with drifter, satellite, and Argo float data, with the primary goal of experimentally assessing the response of the PSSO to the persistent increase of the wind stress over the last two decades. The joint use of in situ and satellite data has proven its effectiveness in several regions of the global ocean. This approach is even more useful in the SO (e.g., Ansorge et al., 2015; Aulicino et al., 2018; Cotroneo et al., 2013) and its marginal seas (e.g., Mangoni et al., 2017; Menna et al., 2019; Misic et al., 2017; Rivaro et al., 2017, 2018, 2019), where in situ data collection is often limited to the summer season and/or affected by the severe sea state and weather conditions. The yearly time series of the EKE field, derived from altimeter data, are compared to the temporal evolution of the zonal wind stress, the ACC baroclinic transport from XBT data, and climate indices (see section 3). Composite maps of EKE derived from drifters are used to define the interannual and decadal variability of the PSSO. Drifter data are also used to obtain estimates of the "divergent component of the meridional EHF"

(hereafter defined as dmEHF) in order to show if the variability of the EKE field affects the poleward eddy heat transport at interannual and decadal scales. To our knowledge, this is the first time that such a large and multiplatform data set has been used to study the PSSO response to the observed variability of the wind stress field, comparing parameters over a range of spatial scales from global to local.

2. Data and Methods.

2.1. EKE From Drifter and Altimetry Data

The Lagrangian drifter data for the period 1995–2017 were downloaded from the Global Drifter Program (GDP) data set distributed by AOML/NOAA, http://www.aoml.noaa.gov/phod/dac/dacdata.php (Figure 2a). Surface Velocity Program (SVP) drifters deployed in this region are particularly affected by the loss of the drogue, resulting in overestimation of the zonal drifter velocity (Grodsky et al., 2011; Rio, 2012; for a discussion on the consequence of the drogue loss on dispersion estimates see Corrado et al. (2017). Therefore, we performed a correction of the drifter velocities for the wind-driven component ($\mathbf{U}_{wind\text{-}driven}$), defined as a sum of direct wind slip (Poulain et al., 2012), Stokes drift, and Ekman currents. $\mathbf{U}_{wind\text{-}driven}$ was estimated following the method of Poulain et al. (2012). Wind velocity gridded data ($\mathbf{W}$: with a spatial resolution of 0.75° and a temporal resolution of 12 hr) were downloaded from the ECMWF ERA-Interim global atmospheric reanalysis (Dee et al., 2011; http://apps.ecmwf.int/datasets/data/interim-full-daily/levtype=sfc/) and interpolated to drifter locations and times. Then, the absolute geostrophic velocities distributed by CMEMS (global, gridded 1/4° Mercator projection.

Grids, daily, delayed time, and quality controlled-CMEMS-SL-QUID_008–032-051) were removed from the drifter velocities $\mathbf{U}$, and the wind-driven component of the drifter velocities was estimated using the regression model proposed by Ralph and Niiler (1999) and Poulain et al. (2012). The relationships between wind-driven currents and wind speed (Table 1) were used to compute $\mathbf{U}_{wind\text{-}driven}$. The SVP drifters with drogue attached measured smaller wind-driven currents, amounting to 0.9% of the wind speed and directed about 33° to the left of the wind; the corresponding explained variance is 7.5%. The SVP without drogue had wind-driven currents of 2% of the wind speed and an angle of 14° to the left of the wind; these drifters tend to move downwind (small angle between the $\mathbf{U}_{wind\text{-}driven}$ and wind directions) because they are significantly conditioned by the wind slip (Menna et al., 2018); these velocities represent 24% of the total velocity variance.

$\mathbf{U}_{wind\text{-}driven}$ currents were subtracted from the drifter velocity measurements to obtain an estimate of the geostrophic components ($\mathbf{U}_{DG} = \mathbf{U} - \mathbf{U}_{wind\text{-}driven}$). Values of $\mathbf{U}_{DG}$ were then used to estimate the EKE fields in bins of 2° × 2° over the PSSO. The velocity residuals were obtained in each bin by subtracting the drifter mean velocity over the period 1995–2017 ($\mathbf{U'}_{DG} = \mathbf{U}_{DG} - \langle \mathbf{U}_{DG} \rangle_{1995-2017}$); therefore, the EKE_{DR} was estimated as $EKE_{DR} = \frac{1}{2}\left(\langle U'^2_{DG} \rangle + \langle V'^2_{DG} \rangle\right)$, where $\langle\rangle$ is the temporal average in each spatial bin. Similarly, the annual residuals of altimetry velocities were obtained in each bin by subtracting the altimetry mean velocity over the period 1995–2017 ($\mathbf{U'}_{SLA} = \mathbf{U}_{SLA} - \langle \mathbf{U}_{SLA} \rangle_{1995-2017}$). These residuals were then used to estimate EKE_{SLA} ($EKE_{SLA} = \frac{1}{2}\left(\langle U'^2_{SLA} \rangle + \langle V'^2_{SLA} \rangle\right)$.

The mean field (1995–2017) of drifter EKEs (EKE_{DR}) and altimeter EKEs (EKE_{SLA}), obtained from the geostrophic current anomalies distributed by CMEMS (derived from the Sea Level Anomaly (SLA) gradients), and the relative standard deviations are shown in Figures 2c–2f. The EKEs calculated from the different data sets show a good qualitative agreement, with the highest values of the standard deviations detected in the region characterized by strong EKEs. Inside the ACC frontal belt, larger EKE values are observed south of New Zealand (between 150°E and 180°W) and in the central PSSO between 120°W and 150°W (Figures 2c and 2e); these regions are characterized by standing ACC meanders (Thompson & Naveira Garabato, 2014; Trani et al., 2014). Outside the frontal belt, large EKE values are associated with migration of eddies, as observed southeast of New Zealand (50°S to 180°W), where the eddies detached from the ACC move northeastward along the steep sides of the Campbell Plateau (Cotroneo et al., 2013). The regions characterized by high values of velocity fluctuations are broader when calculated from drifter data than from the satellite-derived data set. The main causes for this discrepancy are the possible residual wind-driven and nongeostrophic currents measured by drifters (Poulain et al., 2012), the different spatial resolution of the

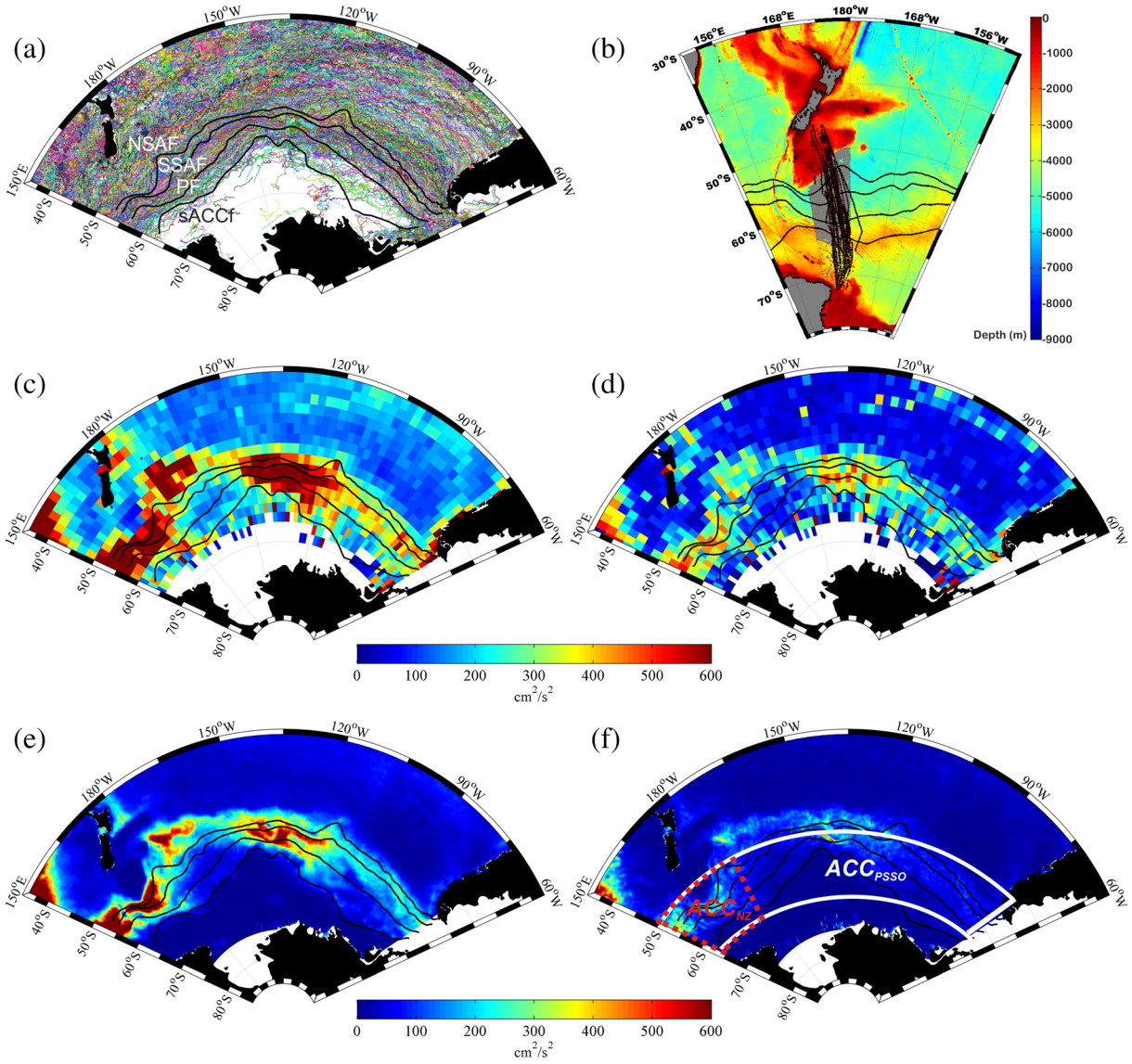

Figure 2. (a) Drifter tracks in the PSSO during the period 1995–2017; black contours show from north to south the mean positions of Northern Sub-Antarctic Front (NSAF), Southern Sub-Antarctic Front (SSAF) and Polar front (PF) (Sallée et al., 2008) and the mean position of the Southern ACC Front (sACCf; Orsi et al., 1995). (b) XBT casts (black dots), Argo float profile positions (gray shaded region south of the Campbell plateau), and bathymetry of the ACC_{NZ} area (colors). (c) Mean EKE fields derived from drifter data and (e) from altimeter data in 1995–2017. (d) EKE standard deviation associated with drifter and (f) altimetry data. The white solid and the red dotted areas in (f) denote the ACC_{PSSO} and ACC_{NZ} sectors, respectively.

two data set, and the spatial smoothing applied to the satellite altimeter data (100-km scale; see Pujol & Larnicol, 2005; Rinaldi et al., 2010). Yearly time series of the EKE_{SLA} and wind stress were estimated over the whole Southern Pacific (between 150°E and 80°W; defined hereafter ACC_{PSSO} sector; white box in Figures 1 and 2f) and over a sector south of New Zealand (between 150°E and 180°W; defined hereafter as ACC_{NZ} sector; red dotted box in Figures 1 and 2f), zonally averaging all the bins located over the ACC (between 50°S and 66°S). Only EKE values ≥80 $cm^2\ s^{-2}$ were considered. The ACC_{NZ} sector has been defined on the basis of available in situ XBT data and on consequent baroclinic transport estimates (Figure 2b).

Table 1
Results of the Regression Model ($\boldsymbol{U}_{wind\text{-}driven} = \beta^{\theta i}\boldsymbol{W}$ + error) Applied to Extract the Wind-Driven Currents From the Drifter Velocities With and Without Drogue; R^2 is the Explained Variance

Drifter type	$\beta^{\theta i}$	R^2 (%)
SVP drogued	0.009exp(33°i)	7.5
SVP undrogued	0.02exp(14°i)	24

High values of spatial standard deviation (Table 2) of the EKE are associated with the large variability between different regions of the study area. As shown in Figure 2d, in the ACC band there are some bins

Table 2
Annual Mean Values of the EKE_{SLA} (≥80 $cm^2\ s^{-2}$) and Corresponding Spatial Standard Deviation Estimated Over the ACC_{PSSO} and ACC_{NZ} Sectors

	EKE ACC_{PSSO} ($cm^2\ s^{-2}$)	Spatial STD ACC_{PSSO} ($cm^2\ s^{-2}$)	EKE ACC_{NZ} ($cm^2\ s^{-2}$)	Spatial STD ACC_{NZ} ($cm^2\ s^{-2}$)
1995	304.2	193.2	487.6	328.4
1996	302.7	186.7	473.5	301.3
1997	311.2	200.1	473.3	311.3
1998	303.0	200.5	496.9	345.1
1999	312.3	208.2	**543.1**	373.0
2000	**333.9**	227.0	**553.5**	373.6
2001	**328.4**	213.5	**521.5**	351.3
2002	313.3	197.9	497.7	309.8
2003	305.5	197.8	477.0	302.1
2004	304.5	197.4	475.6	314.6
2005	308.0	203.1	485.3	330.2
2006	310.2	204.4	471.9	320.83
2007	316.6	205.2	**521.6**	348.5
2008	305.6	195.1	501.3	335.5
2009	**325.2**	209.6	**526.8**	337.5
2010	**319.1**	216.4	494.0	317.4
2011	**327.9**	208.4	**553.1**	349.9
2012	**325.7**	212.3	**538.5**	338.2
2013	**332.4**	223.7	**536.8**	350.1
2014	**338.9**	223.0	**540.5**	358.5
2015	**329.2**	215.7	**523.3**	356.7
2016	**321.9**	213.5	**513.6**	356.0
2017	314.9	208.9	484.7	292.9
Mean (1995–2017)	317.2		508.3	
Temporal (1995–2017) STD	11.2		27.6	

Note. At the end of the table we also provide the mean value and the standard deviation in time over the period 1995–2017 for the EKE evaluated in the two areas. Values larger than the mean values of the time series are written in bold.

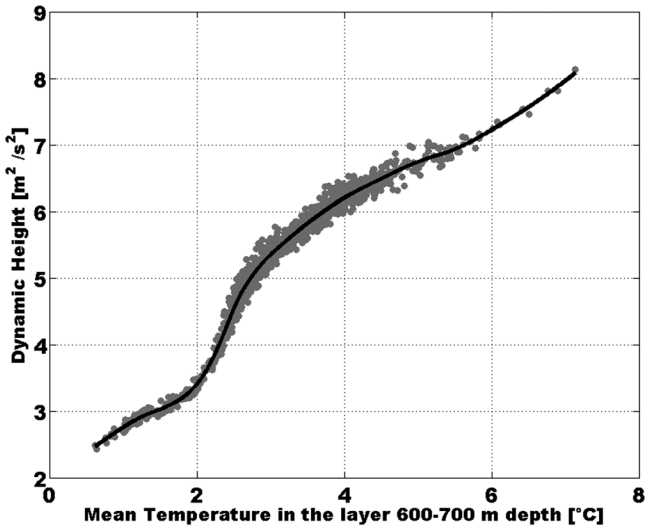

Figure 3. Empirical relation between dynamic height (relative to 2,000 m) and mean temperature in the layer 600–700 m from CTD and Argo float data.

characterized by small EKE (less than 80 $cm^2\ s^{-2}$, located outside the standing meanders) and others characterized by very high EKE values (inside the standing meanders).

Yearly values of the EKE_{SLA} over the ACC_{NZ} sector and the related standard deviations are larger than those observed over the ACC_{PSSO} (Table 2). In order to compare the two time series and fit both into the same plot, we have normalized them by dividing each value by the temporal (1995–2017 defined in Table 2) standard deviation of each time series.

2.2. ACC Baroclinic Transport

An estimate of ACC baroclinic transport relative to 2,000 m was obtained along the New Zealand-Antarctica transect from 1995 to 2017. Following previous investigations in the ACC (Legeais et al., 2005; Rintoul et al., 2002; Sprintall, 2003; Swart et al., 2008), T-S pairs from in situ temperature and salinity data were used to derive an empirical relationship between the mean temperature in the 600- to 700-m layer and the Dynamic Height (DH) relative to 2,000 m (Figure 3).

We obtained this empirical relationship through Argo float and CTD data in the study area from 168°E to 180°E and between 50°S and 70°S (gray shaded area in Figure 2b). Data were downloaded from the CORIOLIS website and then quality controlled through visual inspection to remove any spikes. After that, all profiles collected over the Campbell Plateau were discarded to avoid the presence of data associated with water masses not included in the ACC (Sokolov & Rintoul, 2009). A grand total of 5,829 temperature/salinity profiles from 1992 to 2016 was finally retained.

DH values were then used to estimate the potential energy anomaly, which is a stream function for the baroclinic transport (Rintoul et al., 2002). The obtained transport values are associated with the 2,000-m reference depth and represent an almost constant ratio (61%), of the full depth transport (Rintoul et al., 2002). We will refer to this estimate as "ACC transport."

Through these relationships, we have estimated the baroclinic transport for 25 summer temperature transects collected between New Zealand and Antarctica with XBT probes.

The temperature data originate from a selection of comparable high-density XBT transects between New Zealand and the Ross Sea, carried out by the R/V "Italica" during the austral summers from 1994 to 2017 in the framework of the Italian Antarctic National Programme (Programma Nazionale di Ricerche in Antartide—PNRA; Cotroneo, Budillon, Aliani, Capello, et al., 2018; Cotroneo, Budillon, Aliani, Ferrara, et al., 2018; Cotroneo et al., 2018a, 2018b; Cotroneo, Budillon, Artegiani, Ferrara, 2018; Cotroneo, Budillon, Bergamasco, Capello, et al., 2018; Cotroneo, Budillon, Bergamasco, De Alteris, et al., 2018; Cotroneo, Budillon, Bergamasco, De Stefano, et al., 2018; Cotroneo, Budillon, Castagno, Colizza, et al., 2018; Cotroneo, Budillon, Castagno, De Alteris, et al., 2017; Cotroneo, Budillon, Conversano, 2018; Cotroneo, Budillon, Ferrara, Meloni, Paschini, 2018; Cotroneo, Budillon, Ferrara, Meloni, & Spezie, 2018; Cotroneo, Budillon, Ferrara, Monteduro, 2018; Cotroneo, Budillon, Ferrara, Orsi, et al., 2018; Cotroneo, Budillon, Ferrara, Paschini, 2018; Cotroneo, Budillon, Meloni, et al., 2017). Temperature data along the transect in the layer 0–760 m were collected

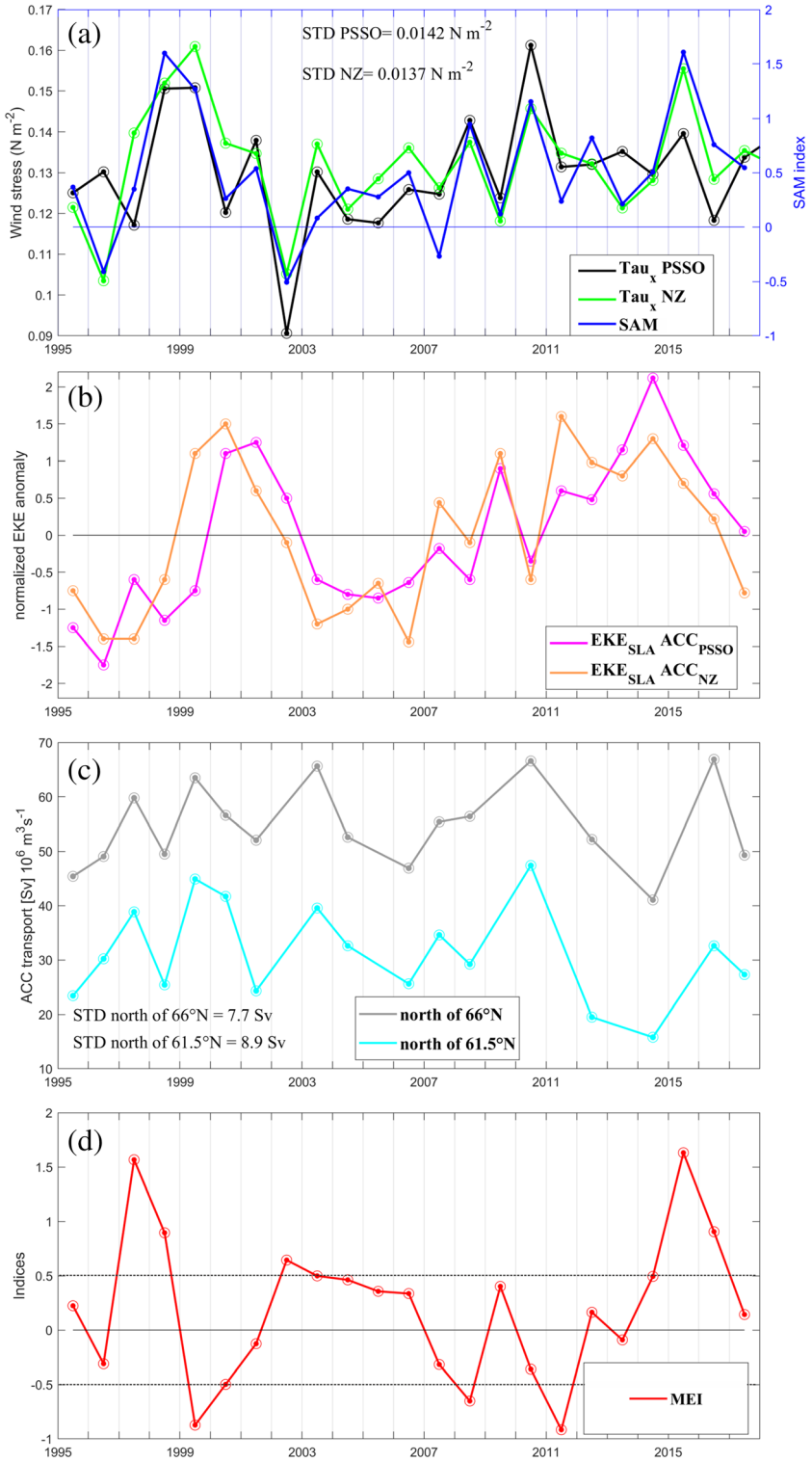

Figure 4. Time series of annual values of (a) the zonal wind stress curl and the SAM index; (b) the normalized anomalies of EKE_{SLA} (obtained by dividing by the values for the temporal STD in Table 2), estimated in the ACC_{PSSO} and ACC_{NZ} sectors; (c) the summer ACC transport from 0- to 2,000-m depth (61% of the full depth transport; see section 3.2) north of 66°N and 61.5°N; (d) the MEI index.

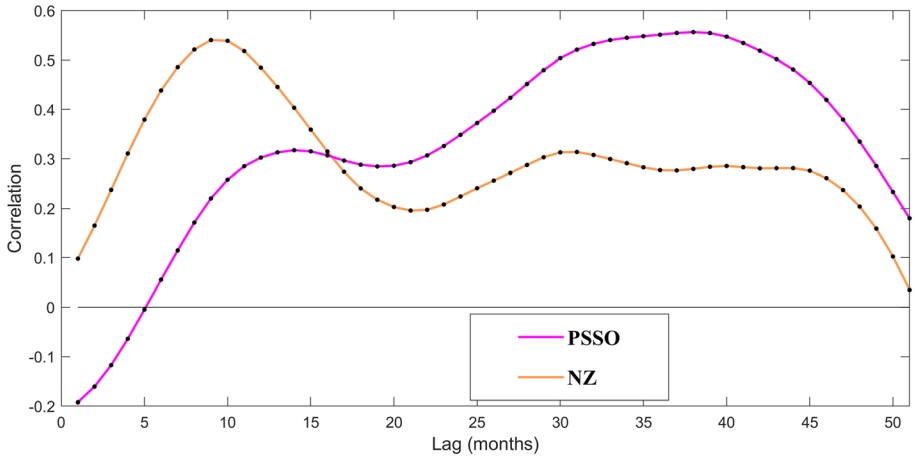

Figure 5. Lagged monthly correlation between the wind stress and the EKE_{SLA} in the PSSO (magenta line) and NZ (orange line) sectors.

at a mean sampling distance of about 28 km. Additional details on the sampling strategy, on the XBT probes, and on the quality control procedure applied to the data can be found in Budillon and Rintoul (2003) and Cotroneo et al. (2013).

In our study, two estimates of the ACC baroclinic transport for each cruise were obtained. In both estimates, the northern limit for the transport calculation was chosen as the latitude of the first available XBT cast south of the Campbell Plateau, where the ACC is expected to flow, as its fronts are deep-reaching features and tend to wrap around bathymetric features shallower than 2000 m (Sokolov & Rintoul, 2009). Two possible southern limits of integration for the ACC transport were tested: 61.5°S is the mean position of the PF in the area (Budillon & Rintoul, 2003), and 66°S represents the possible southernmost extension of any flow associated with the ACC. This is because, in our study area, any data collected at higher latitudes may be influenced by more local dynamics associated with the Antarctic zone of the ACC.

Even if the used data set can be considered evenly distributed in space and time, with at least one transect during each austral summer from 1995 to 2017, some years have been excluded by the transport time series due to significant track changes caused by severe weather conditions, (i.e., 2002, 2005, and 2015) or incomplete or unrealized sampling along the transect (i.e., 2009 and 2011). Considering the lack of data in some years and averaging the transport estimates obtained during the same austral summer, 17 transport values were obtained for the two considered latitudinal bands.

2.3. Wind Stress Estimations

The ERA-Interim wind velocities described in section 3.1 were used to quantify the wind stress. The drag coefficient employed for this estimation is defined in Yelland and Taylor (1996) using a wide range of wind speeds over the SO. Yearly time series of the wind stress were estimated over the ACC_{PSSO} and ACC_{NZ} sectors (Figure 4b). Monthly time series of the wind stress were also lag correlated with monthly time series of EKE_{SLA} (Figure 5).

2.4. Climatic Indices

The time series of the wind stress and EKE_{SLA} were compared with the temporal evolution of the SAM index (Marshall, 2003; https://climatedataguide.ucar.edu/climate-data/marshall-southern-annular-mode-sam-index-station-based) and of the multiparametric Multivariate-ENSO Index (MEI; https://www.esrl.noaa.gov/psd/enso/mei/) (Wolter & Timlin, 1993, 1998, 2011) used to define the phases of SAM and ENSO, respectively. Negative values of the MEI represent the cold ENSO phase (La Niña events), while positive MEI values represent the warm ENSO phase (El Niño events). Absolute values between 0.5 and 1.0 are defined as moderate El Niño (moderate La Niña if the MEI is negative), whereas absolute values larger than 1 are defined as strong El Niño (strong La Niña if the MEI is negative) (Seymour, 2008).

2.5. Meridional EHFs

Near-surface EHF was estimated using the velocity residuals and the residual fluctuation of the sea surface temperature (performed dividing winter and summer data) measured by drifters, following the method of Trani et al. (2011). The meridional EHFs $<v'T'v'T'>$, where $\langle\rangle$ is the spatial mean in each bin, namely, the covariance of the meridional component of the velocity residuals (v') and of the temperature residual fluctuation (T'), were divided in their rotational and divergent components. The rotational component does not contribute to the globally integrated poleward heat transport by the ocean and is not considered in this work, whereas the divergent component (dmEHF) affects the local heat budget (Marshall & Shutts, 1981; Trani et al., 2011) and is of considerable dynamical interest (Jayne & Marotzke, 2002).

The dmEHF values were evaluated in bins of 5° longitude by 2.5° latitude. Velocity residuals v' were obtained by subtracting the 23-year mean of the meridional velocities from each value of the meridional velocity in each bin, then filtered with a 48-hr low-pass second-order Butterworth filter to remove the high-frequency components. Two different 23-year temperature averages were estimated, a summer mean (October–March) and a winter mean (April–September), then subtracted selectively in each bin from the summer/winter bin values. In this way, the final mean in each bin considers the strong seasonal variability of the temperature in the SO.

Interannual maps of dmEHF, EKE_{DR} anomalies (defined with respect to the mean field of EKE_{DR} in 1995–2017), and EKE_{SLA} anomalies (defined with respect to the mean field of EKE_{SLA} in 1995–2017) were estimated in the period characterized by positive (2000–2002, 2009, and 2011–2017) and negative (1995–1999 and 2004–2008) anomalies of EKE_{SLA} (defined hereafter as EKE^{+} and EKE^{-}, respectively, with the eventual addition of the subscript $_{DR}$ or $_{SLA}$ according to the data set used) and for the two decades 1995–2006 and 2007–2017. The decades were selected according to three goals: (1) to make a comparison between the period 1995–2006 as analyzed by Trani et al. (2011, 2014) and the following decade (2007–2017), (2) to compare two periods where the EKE_{SLA} anomaly shows very different characteristics and assess how and if these differences affect the distribution and intensity of the dmEHF, and (3) to compare a period in which the SAM index is always positive (2007–2017) with a period (1995–2006) in which it shows 2 years with negative values. Bins with less than 100 observations are not considered.

Hereafter, southward/poleward dmEHF will be defined as "negative", whereas northward/equatorward dmEHF will be defined as "positive."

3. Results

3.1. Analysis of the Annual Averaged Time Series

The time series of the annual averaged zonal wind stress over the ACC_{NZ} and the ACC_{PSSO} sectors (Figure 4a) show a yearly variability generally in phase over both areas. Two exceptions are observed in 1996 and 2013, when the local response of the wind stress (Tau_x NZ in Figure 4a) is out of phase with respect to the PSSO. The comparison between the temporal evolution of the SAM index and the amplitude of the zonal wind stress (Figure 4a) confirms that the SAM represents the variability of the circumpolar wind stress, in agreement with Meredith and Hogg (2006). The SAM index shows significant correlations ($p < 0.05$; confidence level 95%) and a high coefficient of correlation with both Tau_x NZ (0.84) and Tau_x PSSO (0.71). In 1996 and 2013 the SAM index is in phase with the wind stress in the NZ sector.

The time series of the yearly normalized average EKE_{SLA} fields (Figure 4b) are characterized by two dominant peaks that occurred in the ACC_{PSSO} sector in 2001 and 2014 and in the ACC_{NZ} sector in 2000 and 2011. EKE_{SLA} values are generally larger in the ACC_{NZ} sector (see Table 2), where one of the ACC standing meanders is located, with respect to the ACC_{PSSO} sector, where the mean calculation includes ACC regions inside and outside the meanders (Figures 2c and 2e). Despite these differences in amplitude, the two time series show a congruent temporal evolution (Figure 4b). The coefficient of correlation of 0.81 ($p < 0.05$; confidence level 95%) indicates that the time series of EKE_{SLA} in the ACC_{PSSO} and ACC_{NZ} sectors are mutually comparable, as is also seen with the wind stress field. Consequently, we assume that the estimation of the ACC transport south of New Zealand is representative of the PSSO transport. Table 2 summarizes the annual values of EKE_{SLA} in the two sectors as well as the corresponding annual (spatial mean on the ACC_{PSSO} and ACC_{NZ} sectors) and total (temporal mean; 1995–2017) standard deviations.

The time series of the ACC transport (Figure 4c) were calculated using the two different southern limits (see section 3.2): 66°S ($ACC_{66°S}$; black curve) and 61.5°S ($ACC_{61.5°S}$; cyan curve). The choice of two southern limits (previously described) also allows us to analyze the contribution to the variability coming from the southern fronts, which, according to the "free mode" response (Hughes et al., 1999) of the ACC to increasing wind stress, responds quicker than do the northern fronts. Hughes et al. (1999) used barotropic vorticity balance arguments to demonstrate that the wind is correlated at near-zero time lag with the total ACC transport in the southern sector of the current. The immediate response of the ACC transport associated with the southern fronts to the wind stress is due to the rapid propagation of barotropic waves (Webb & De Cuevas, 2007). Including the southern fronts, the magnitude of transport increases (the transport estimated using 66°S as southern limit is larger than that obtained using 61.5°S) but the two time series of the ACC transport reveal relatively little variability over the decadal time scale, in agreement with some works focused on the variability of the baroclinic transport in the Drake Passage (e.g., Hogg et al., 2015; Meredith et al., 2011). On the other hand, at interannual time scales the ACC transports show substantial variability. The interannual variability is relatively insensitive to the southern limit used to estimate the transport as the observed oscillations are in phase and with limited variability of the differences between the two estimates over the study period. The largest difference is found in 2016 when only the $ACC_{66°S}$ transport is significantly larger than its mean value.

3.2. Influence of the Wind Stress on the Variability of the EKE Field in the PSSO

The comparison between the time series of the zonal wind stress (Figure 4a) and the anomaly of EKE_{SLA} (Figure 4b) shows increasing values of the EKE field that follow the peaks of the wind stress. The first event of positive EKE_{SLA} occurs in 2000–2002 in the ACC_{PSSO} (magenta line; Figure 4b) and in 1999–2001 in the ACC_{NZ} (orange line; Figure 4b) and lags the peaks of Tau_x by ~2 years in the ACC_{PSSO} sector and ~1 year in the ACC_{NZ} sector. The delays observed in the ACC_{PSSO} sector agree with those discussed in previous studies (e.g., Langlais et al., 2015; Meredith & Hogg, 2006; Morrow et al., 2010). The second event of positive EKE_{SLA} in both sectors is observed in 2009 (Figure 4b), 1 year after the peaks of Tau_x (Figure 4a). The third event, related to the peaks of Tau_x in 2010 (Figure 4a), is followed by high positive values of EKE_{SLA} in the period 2011 to 2016 in both sectors (Figure 4b). The ACC_{NZ} sector shows the larger peak of EKE_{SLA} in 2011 (Figure 4b), 1 year later than the peak of Tau_x, whereas in the ACC_{PSSO} sector the larger peak is observed in 2014, about 4 years later than the peak of Tau_x. Therefore, the ACC_{NZ} sector (orange line; Figures 4b and 5) responds to the wind stress earlier than the entire PSSO (magenta line, Figure 4b and 5), showing larger correlations 9–10 months later than the wind stress peak. The ACC_{PSSO} sector shows a relative maximum in the correlation ~15 months later than the wind stress peak and the absolute maxima 35 months later (Figure 5). These results agree with the conclusions by Morrow et al. (2010), who observed an increase in the delay of the EKE signal peak with respect to the SAM index moving from west to east in the Pacific. Furthermore, the delay between the EKE_{SLA} peaks in the two ACC sectors could stem from the local increase of the EKE_{SLA} in the ACC_{NZ} sector achieved by the standing meander located in this area. As described by Thompson and Naveira Garabato (2014), there is a different behavior of the EKE (in phase and amplitude) in the local standing meanders of the ACC with respect to the regional response.

All the above-mentioned peaks of Tau_x (1998–1999, 2008, and 2010), associated with consequent increases of the EKE_{SLA}, are concurrent with negative values of MEI (La Niña events in the tropical Pacific Ocean; Figure 4d). In 2015, a significant increase of Tau_x is observed only in the ACC_{NZ} sector, concurrent with a strong positive MEI (El Niño event in the tropical Pacific Ocean; Figure 4d); in this condition, no evident influences on the EKE_{SLA} are observed.

Negative anomalies of EKE_{SLA}, related to the reductions of Tau_x (Figure 4a), are observed in the period 1995–1998 and 2002–2006 in the ACC_{NZ} sector and in 1995–1999 and 2003–2008 in the ACC_{PSSO} sector (Figure 4b).

3.3. Interannual and Decadal Variability of the EKE Field

Interannual maps of EKE^{+}_{DR}, EKE^{-}_{DR}, and EKE^{+}_{SLA}, EKE^{-}_{SLA} anomalies (see definitions in section 2.5) provide an overview of the spatial distribution of the EKE field over the whole PSSO (Figure 6). The western

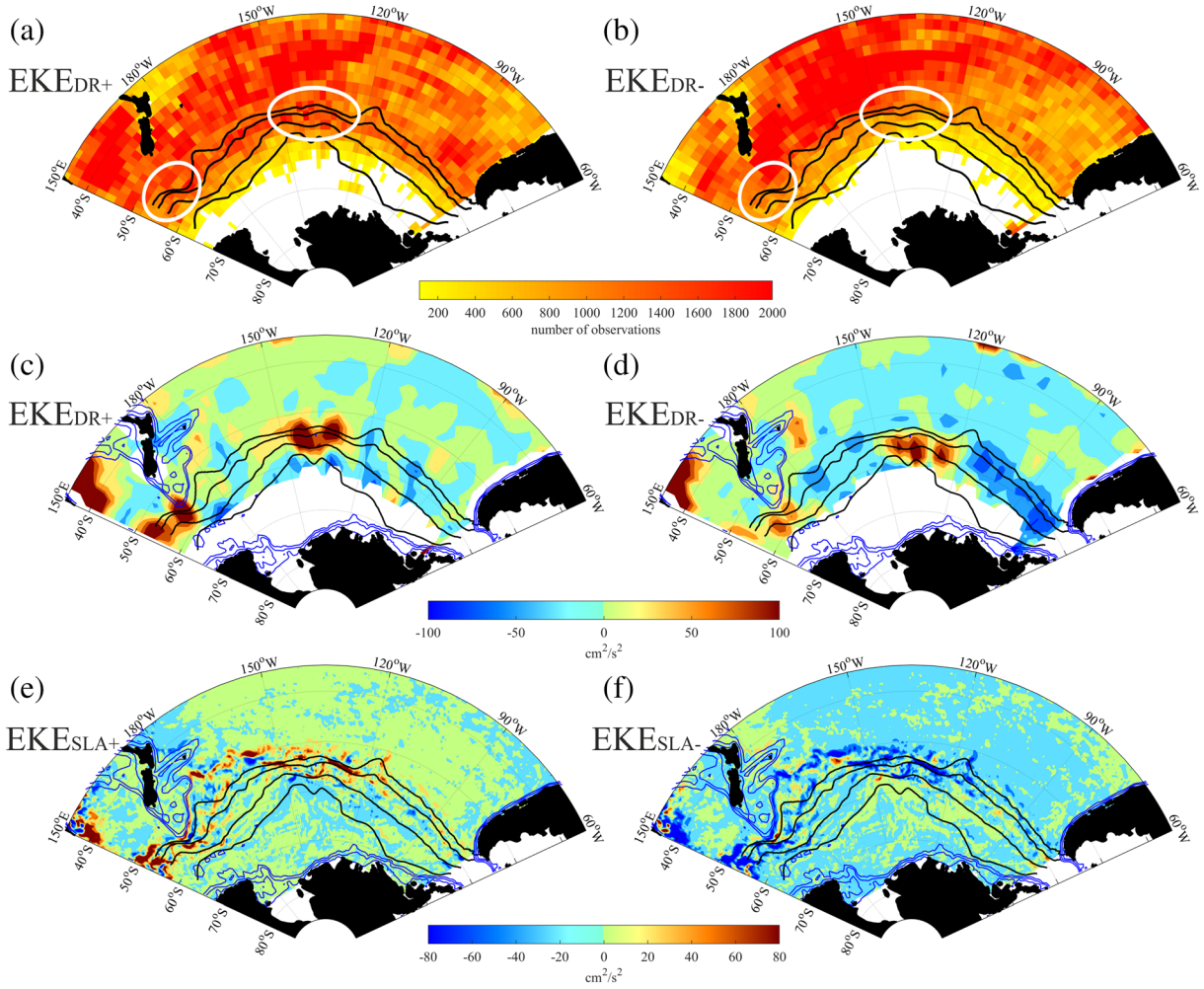

Figure 6. Spatial distribution of the number of observations in bins of 2° × 2° over the period EKE^{+}_{DR} (a) and EKE^{-}_{DR} (b). Interannual maps of the anomalies of EKE^{+}_{DR} (c), EKE^{-}_{DR} (d), EKE^{+}_{SLA} (e), and EKE^{-}_{SLA} (f). Black contours show the mean positions of NSAF, SSAF, PF, and sACCf (see Figure 2). White circles in panels (a, b) show the mean location of the stranding meanders in PSSO. Blue lines in panels (c–f) describe the 500, 1,000, 1,500, 2000, and 2,500 m isobaths.

sector is more extensively sampled by drifter than the eastern one (Figures 6a and 6b), and the ACC band is better sampled during the $EKE_{SLA}{}^{+}$ period.

The EKE field strengthens during the EKE^{+}_{DR} in the whole PSSO, with larger positive anomalies along the ACC pathway (Figures 6c and 6d). The positive anomalies of EKE^{+}_{DR} exceed 400 $cm^2\ s^{-2}$ in the standing meander of the ACC_{NZ} sector and are in the range of 200–300 $cm^2\ s^{-2}$ in the central meander of the ACC_{PSSO}. Negative anomalies of EKE^{-}_{DR} are observed in the ACC_{PSSO} sector inside and outside the ACC pathway (Figure 6d). Larger positive EKE^{-}_{DR} anomalies persist in the standing meanders of the ACC (with values lower than 200 $cm^2\ s^{-2}$) and in the region where the eddies detached from the Campbell Plateau (about 50°S to 180°W; see Figures 6d and 1 for the geographical location of the Campbell Plateau). The qualitative comparison between EKE_{DR} (Figures 6c and 6d) and EKE_{SLA} (Figures 6e and 6f) over the whole PSSO shows a good agreement between the two data sets both during EKE^{+}_{SLA} and EKE^{-}_{SLA}. The positive anomalies described by EKE_{DR} in the central meander of the ACC_{PSSO} during EKE^{-}_{SLA} periods are located further south (along the sACCf) in the altimetry data set. More generally, the ACC standing meanders are better highlighted by drifter than by altimetry data.

The number of drifter observations in the PSSO rises with time showing the expected increase during the decade 2007–2017. (Figures 7a and 7b). Beyond the differences in sampling, in both decades the EKE_{DR} fields (Figures 7c and 7d) agree with the EKE_{SLA} fields (Figures 7e and 7f).

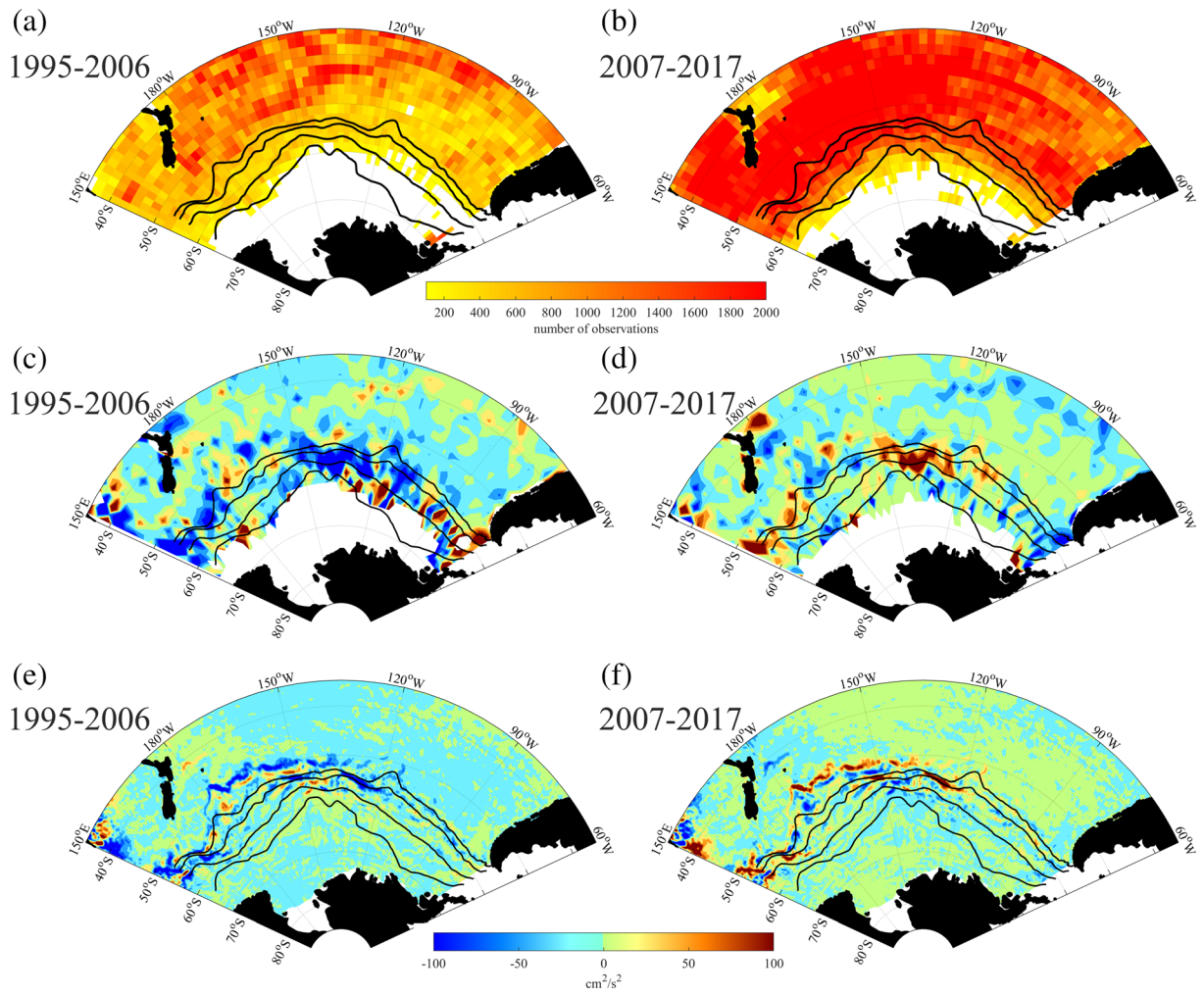

Figure 7. Spatial distribution of the number of observations in bins of 2° × 2° over the period 1995–2006 (a) and 2007–2017 (b). Interannual maps of the anomalies of EKE_{DR} (c, d) and EKE_{SLA} (e, f) over the years 1995–2006 (c, e) and 2007–2017 (d, f). Black contours show the mean positions of NSAF, SSAF, PF, and sACCf (see Figure 2).

At decadal time scales, larger changes of the EKE_{DR} mainly occurred in the ACC band (Figures 7c and 7d), characterized by negative EKE anomalies during the first decade (only the longitudinal sector 180–150°W shows positive anomalies) and positive anomalies during the 2007–2017 decade. This increase is consistent with the increase of the wind stress, as also pointed out by Hogg et al. (2015). The increase/decrease of the EKE anomalies is larger for EKE_{DR} than for EKE_{SLA}. In the latter case, (Figures 7e and 7f) the transition between the two decades is smoother and the strongest variations occurred along the SSAF and NSAF.

3.4. Interannual and Decadal Variability of the Divergent Component of the Meridional EHFs

Southward dmEHF balances the heat loss at high latitudes in the SO. We calculated the dmEHF using velocity and SST data derived from drifters as described in section 3 and in Trani et al. (2011). Due to their Lagrangian nature, drifters move with the currents providing an accurate but irregular spatial and temporal sampling of the near-surface currents and SST. For this reason, yearly time series of dmEHF would not be statistically robust (in some years there is a limited number of observations and/or the observations are located only in a specific area of the PSSO). Nevertheless, the multiyear statistics are robust and reliable enough to study if the dmEHF are sensitive to the EKE^{+} and EKE^{-} periods. To build the composite EKE^{+} and EKE^{-} maps, we selected the dmEHF value in the same years already selected for the EKE field (section 3.4). The averaged dmEHF maps are also estimated for the two decades as done for the EKE field.

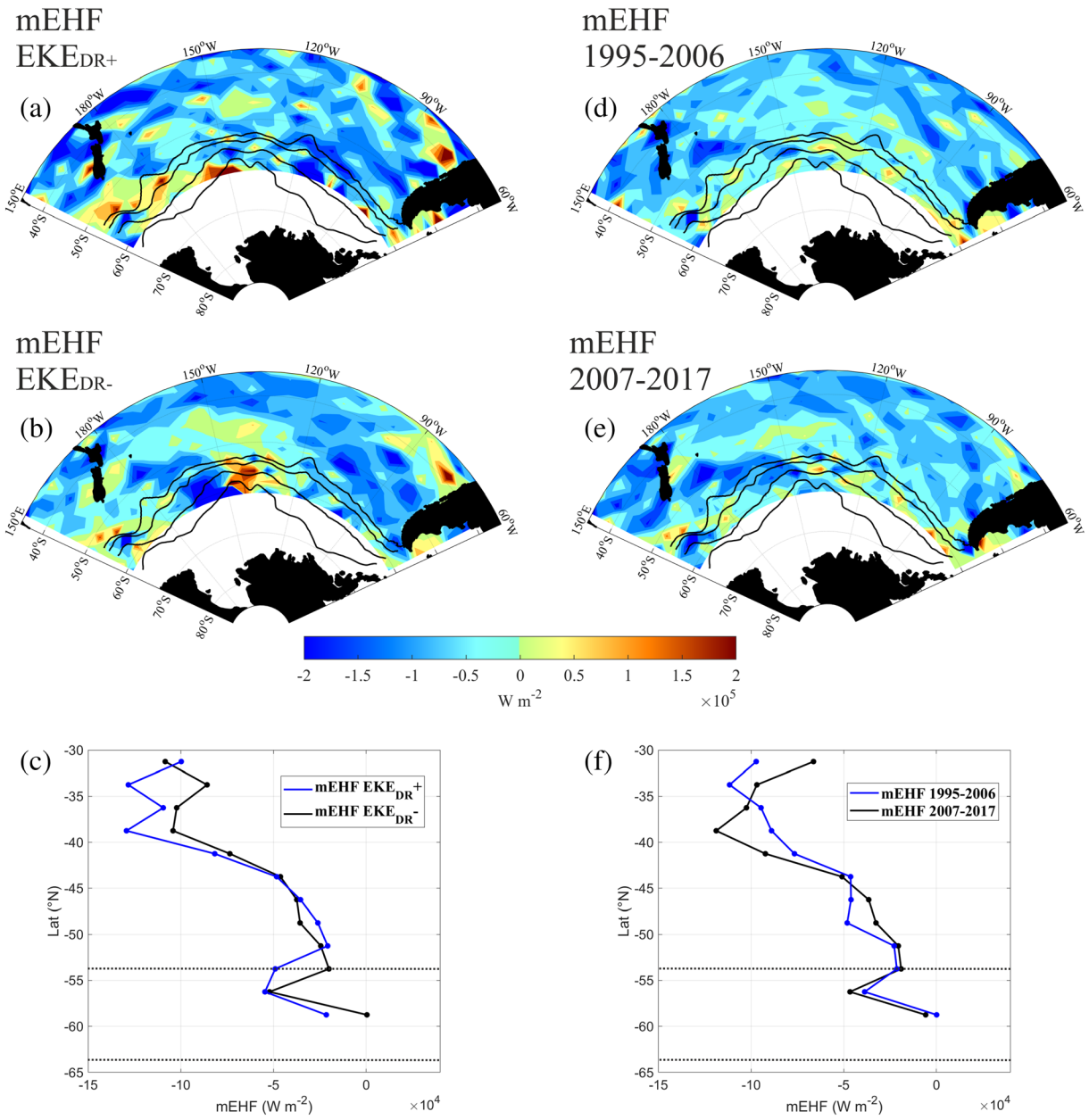

Figure 8. Interannual meridional component of the divergent eddy heat fluxes during EKE^+ (a) and EKE^- (b) periods. Zonally averaged meridional component of the divergent eddy heat fluxes during EKE^+ and EKE^- periods (c). Interannual meridional component of the divergent eddy heat fluxes during 1995–2006 (d) and 2007–2017 (e) periods. Zonally averaged meridional component of the divergent eddy heat fluxes during 1995–2006 and 2007–2017 periods (f). Black contours in panels (a, b, d, and e) show the mean positions of NSAF, SSAF, PF, and sACCf (see Figure 2). Black dashed lines in panels (c, f) define the northern and southern geographical limits of the ACC band, that is, the mean location of the NSAF and sACCf, as described in Cotroneo et al. (2013).

The dmEHF is predominantly negative both during the EKE^+ and EKE^- periods (Figures 8a and 8b), with a strengthening of the dmEHF field during EKE^+, both with positive and negative values (Table 3). Negative dmEHF is distributed over the whole PSSO in the EKE^+ period, sometimes interrupted by small areas characterized by weak positive values. High positive values are observed south of New Zealand, downstream of the South Pacific Ridge, and in the northeastern region of the PSSO (west of the South American coast). During the EKE^- period, there is a large region characterized by positive dmEHF in the middle of the PSSO (south of 40°S and between 130°W and 160°W) with maximum positive values in the ACC latitudinal band.

Table 3
Sum of the Positive and Negative Contributions of the dmEHF Over the PSSO During the EKE_{DR}^{+} and EKE_{DR}^{-} Periods and Over the 1995–2006 and 2007–2017 Periods

	Sum of positive dmEHF (W m^{-2})	Sum of negative dmEHF (W m^{-2})
$EKE+_{DR}$	2.86e + 7	−8.05e + 7
EKE^{-}_{DR}	2.19e + 7	−7.22e + 7
1995–2006	1.59e + 7	−6.39e + 7
2007–2017	1.52e + 7	−6.49e + 7

The latitudinal evolution of the dmEHF (obtained zonally averaging the values in Figures 8a and 8b) shows negative mean values over the whole PSSO in both the periods, decreasing in magnitude moving from north to south (Figure 8c). Periods of EKE^{+} shows larger negative mean values than for EKE^{-}, especially north of 40°S and in the ACC latitudinal band (between 50°S and 60°S).

The distribution of the dmEHF at decadal time scales is shown in Figures 8d and 8e, and the sum of positive and negative contributions for the PSSO is provided in Table 3. Small differences are found between the two decades, despite the increase in EKE observed since 2006 (Figures 4 and 7). The zonally averaged dmEHF over the two decades (Figure 8f) show a pattern like the observed in Figure 8c, and it confirms a trend toward more negative dmEHF from 50°S to 56°S. The increase of the dmEHF in the band of the ACC (Figures 8c and 8f) is in agreement with the results of Sun et al. (2019) derived by Argo float data in the first 1,000-m depth of the water column. It is interesting to note that, even though the first decade is less sampled than the second one (Figures 7a and 7b), it still provides a latitudinal evolution consistent with the other periods (Figures 8c and 8f).

4. Discussion

The PSSO is a region of the SO that is strongly influenced by the increase of the wind stress observed during the last two decades (Hande et al., 2012; Hogg et al., 2015; Lin et al., 2018; Morrow et al., 2010; Patara et al., 2016). This work explores some of these aspects using an extensive data set of oceanographic in situ data collected in the PSSO between 1995 and 2017 and the wind stress field from the ERA-Interim reanalysis.

The time series of the zonal wind stress and eddy field derived from altimetry have been analyzed in the PSSO, focusing on the ACC latitudinal band. They show three periods of positive EKE_{SLA} anomaly associated with an increase of the wind stress (Figures 4a and 4b). The response of the eddy field is lagged by about 1–2 years with respect to the wind stress peaks. Periods of positive EKE_{SLA} anomalies are always preceded by La Niña events in the equatorial region of the Pacific Ocean (negative MEI values being observed in 1999, 2008, and 2011; Figure 4c). On the other hand, strong El Niño events (MEI values larger than 1 in 1997 and 2015) are related to decreasing or negative anomalies. A mainly positive state of SAM index (Figure 4a) characterizes the entire period analyzed in this work; negative events were observed only in 1996 and 2002. These considerations suggest a connection between the interannual variabilities of large-scale indices and regional parameters. ENSO develops in the equatorial region of the Pacific Ocean, influencing the strength of the atmospheric pressure field that, in turn, acts to modulate the pressure gradient between the tropical and high-latitude zones and then the wind field (Fogt et al., 2011; Fogt & Bromwich, 2006). The influence of a persistent wind intensity increase (associated with a SAM index > 0) on the EKE field can be thus modulated by the ENSO phase. Some examples of this effect are given in the time series of Figure 4: (1) The two highest wind stress peaks over the PSSO (1998 and 2010) are associated with SAM index > 0 and MEI < 0 followed by an increase in EKE; (2) the lowest wind stress value (in 2002) is associated with SAM index < 0 and MEI > 0, followed by a decrease of EKE; and (3) despite the high positive SAM index in 2015, the occurrence of the "super" El Niño in the same year determines a relatively weak wind field and a following EKE decrease. The connections between the interannual variability of the wind stress and large-scale indices and of regional parameters have been extensively investigated in the literature, defining how the interaction between SAM index and ENSO can influence the general SO circulation (Cerrone, Fusco, Cotroneo, et al., 2017), its sea ice cover (Cerrone, Fusco, Simmonds, et al., 2017; Cerrone & Fusco, 2018), its mixed layer depth (Buongiorno Nardelli et al., 2017), and even the surface heat fluxes at regional scales (Fusco et al., 2018). Recently, Silvano et al. (2020) demonstrated how the combined effect of the ENSO and the SAM state can affect the sea ice formation in the Ross Sea, explaining the recent reversal of the salinity trend observed in the Ross Sea (Castagno et al., 2019). The ability of El Niño to mitigate the effect of the strong SAM is already described by Morrow et al. (2010), Fogt et al. (2011), and Langlais et al. (2015). Very likely, other factors influence the states and the PSSO response (e.g., the natural and intrinsic variability or the role

of standing meanders), but we do not have enough information and data to figure out the respective contributions to the overall variability.

Contributions to the total ACC transport variability come from the barotropic component (that we cannot calculate using our data), Ekman transport (that is beyond the scope of this work), and from the baroclinic transport of the ACC. In this work, we realized two estimates of the total baroclinic transport south of New Zealand (Figure 4c) for two different latitudinal bands. Each estimate is referred to 2,000-m depth and represents a fraction (61%) of the full depth transport associated with the ACC. Our estimates show interannual variability, but no remarkable differences can be noticed over the whole study period. However, over the whole study period, the ACC transport does not change, and the variability is almost the same for both the southern limits we have chosen. Our estimate of the baroclinic transport agrees with the results found by Langlais et al. (2015), who applied two different models along a section south of New Zealand. The two estimates are in agreement in the period in which the time series can be overlapped (from 1995 to 2007), both for the total value (see Figure 4d of Langlais et al., 2015) and for the variability (Figure 5d in Langlais et al., 2015), also considering the different time resolution of the calculated transport.

Based on the EKE and baroclinic transport time series, the PSSO behavior is consistent with an eddy saturation response. Two events at decadal time scale are observed, namely, after the 1999 and 2010 wind stress peaks (Figure 4a), followed by EKE maxima in 2002 and 2014 (Figure 4b). In both cases, the wind stress increase does not significantly change the transport but instead enhances the eddy field. The time lag is consistent with estimates already by Meredith and Hogg (2006), Morrow et al. (2010), and Hogg et al. (2015). On the other hand, two decades of data represent a still short time series to assess the dynamical response of the ACC to the changing wind at a decadal time scale. Longer time series and model analysis are still needed to address this crucial point.

The influence of the increasing EKE in the PSSO and in the SO in general (e.g., Hogg et al., 2015) on the dmEHF has been addressed in the literature. According to previous studies, the increase of EKE facilitates the meridional heat transport with broader implications for global climate (Hogg et al., 2008; Sallée et al., 2008). Additional studies (e.g., Treguier, 2010) have shown that trends in EKE do not necessarily imply similar trends in the dmEHF. Recently, Foppert et al. (2017) showed that long-term increases in the dmEHF are significantly related to the change in wind stress and to the increase of EKE in two main hot spots, namely, the Kerguelen Plateau and the Southwest Indian Ridge.

In our study, we have shown that the distribution of dmEHF describes an enhancement of poleward heat fluxes during the years with EKE^{+} (Table 3 and Figures 8a and 8c) and dominant equatorward fluxes in the central region of PSSO (south of 40°S, 130–160°W) during EKE^{-} with maximum positive values in the ACC latitudinal band (Figure 8b). The poleward dmEHF generally decreases moving to the south, but a local increase is observed in the band of the ACC (Figures 8c and 8f) that is probably related to the strong increase in the EKE_{SLA} in this area (Figures 2c and 2e). This behavior is also observed in the dmEHF derived by Sun et al. (2019) using Argo float data. There are no clear hot spots in the PSSO in the area upstream and downstream of the South Pacific Ridge, in both EKE^{+} and EKE^{-} periods, in agreement with Foppert et al. (2017). South of New Zealand, where the ACC meanders, is observed an area with dmEHF > 0, especially in EKE^{+} period when it extends over the Campbell Plateau. Values of dmEHF > 0 can be found only along the NSAF in EKE^{-} period.

The absence of large differences in dmEHF between the first and second decades, even though the two decades are very different in terms of EKE, could be due to the presumed delay between cause and effect that cannot be observed through our data set. Hogg et al. (2008), using an eddy-resolving quasi-geostrophic model of the wind-driven circulation, show that the southward shift of the westerlies produces an initial cooling (due to the northward Ekman transport), but the long-term response of the SO is a warming, more intense in the southern sector of the ACC. This lagged effect showed by Hogg et al. (2008) is based on the assumption that the SO is in eddy saturation state. They also indicate values of 3–6 years for the time lag between the increase of the wind and the increase of SST, but there are no indications on how this lag and the EKE lag are related. On the other hand, the suggested lag between the peaks of EKE and the response of the dmEHF can affect our estimate of the decadal dmEHF (Figure 8).

The irregular spatial and temporal drifter sampling does not allow producing robust yearly statistics of the dmEHF. It is difficult to compare our results with other works due to different time and spatial resolution of drifter data in the PSSO. However, the meridional averaged dmEHF agree well with previous studies (Gille, 2003; Jayne & Marotzke, 2002; Sun et al., 2019; Trani et al., 2011), both in terms of magnitude and pattern.

5. Conclusions

Using an extensive data set of oceanographic observations collected in the Pacific Sector of the Southern Ocean (PSSO), we studied how this sector of the SO is responding to the wind stress field increase occurring over the last decades. The response of the PSSO is defined in terms of temporal evolution of the baroclinic transport, the EKE field, and the possible changing in the divergent component of the meridional Eddy Heat Fluxes (dmEHF).

Our main findings are as follows:

1. The EKE field increases over the study period, especially from 2007;
2. The baroclinic component of the ACC transport shows no trend over the whole period, even though interannual variability appears significant;
3. The PSSO shows a response that is consistent with a state of eddy saturation at decadal time scale;
4. dmEHF values increase during EKE^{+} period, but no significant variation was observed between the two decades.

To further investigate some of these aspects, it is desirable in the future to compare the estimates of the baroclinic transport south of New Zealand with those obtained along other transects of the Antarctic region. A second aspect worth exploring will be the possible delay between the increase in EKE and the distribution of dmEHF, which should be reconstructed with the help of numerical models and/or with the use of satellite temperature and current data. Finally, a third aspect to investigate will be the contribution of the intrinsic ocean variability to the dynamic and heat balance in the SO.

Data Availability Statement

Quality controlled data are available on the morsea.uniparthenope.it website. XBT data from 1994 to 2012 can be also downloaded through the National Centers for Environmental Information database of the NOAA (https://www.nodc.noaa.gov/archivesearch/catalog/search/search.page, keyword: italica). CTD and Argo Data were collected and made freely available by the Coriolis project and programs that contribute to it (http://www.coriolis.eu.org). Drifter data can be downloaded online (http://www.aoml.noaa.gov/envids/gld/index.php).

Acknowledgments

The XBT data were collected in the framework of the CLIMA, CLIMA IV, SoChIC, MORSea projects supported by the Italian National Program for Antarctic Research-PNRA, which provided financial and logistic support. We thank the officers, crew, and technical personnel on board the R/V Italica for their support during the seagoing operations. Part of drifters and floats data are collected in the framework of Argo Italy program, under the sponsorship of the MIUR (Italian Ministry of University and Research). In situ data analysis was performed in the framework of the MOMA, MORSea, and ACCUA projects of the PNRA. This work was partly funded by the Parthenope University Individual and Group Research funds.

References

Abernathey, R. P., & Cessi, P. (2014). Topographic enhancement of eddy efficiency in baroclinic equilibration. *Journal of Physical Oceanography*, *44*(8), 2107–2126. https://doi.org/10.1175/JPO-D-14-0014.1

Ansorge, I. J., Jackson, J. M., Reid, K., Durgadoo, J. V., Swart, S., & Eberenz, S. (2015). Evidence of a southward eddy corridor in the south-west Indian ocean. *Deep Sea Research, Part II*, *119*, 69–76. https://doi.org/10.1016/j.dsr2.2014.05.012

Aulicino, G., Cotroneo, Y., Ansorge, I., van den Berg, M., Cesarano, C., Belmonte, M., & Olmedo, E. (2018). Sea surface salinity and temperature in the southern Atlantic Ocean from South African icebreakers, 2010-2017. *Earth System Science Data*, *10*(3), 1227–1236. https://doi.org/10.5194/essd-10-1227-2018

Budillon, G., & Rintoul, S. R. (2003). Fronts and upper ocean thermal variability south of New Zealand. *Antarctic Science*, *15*(1), 141–152. https://doi.org/10.1017/S0954102003001135

Buongiorno Nardelli, B., Guinehut, S., Verbrugge, N., Cotroneo, Y., Zambianchi, E., & Iudicone, D. (2017). Southern Ocean mixed layer seasonal and interannual variations from combined satellite and in situ data. *Journal of Geophysical Research: Oceans*, *122*, 10,042–10,060. https://doi.org/10.1002/2017JC013314

Castagno, P., Capozzi, V., Di Tullio, G. R., Falco, P., Fusco, G., Rintoul, S. R., et al. (2019). Rebound of shelf water salinity in the Ross Sea. *Nature Communications*, *10*(1), 5441. https://doi.org/10.1038/s41467-019-13083-8

Cerrone, D., & Fusco, G. (2018). Low-frequency climate modes and Antarctic sea ice variations. 1982–2013. *Journal of Climate*, *31*, 147–175. https://doi.org/10.1175/JCLI-D-17-0184.1

Cerrone, D., Fusco, G., Cotroneo, Y., Simmonds, I., & Budillon, G. (2017). The Antarctic circumpolar wave: Its presence and interdecadal changes during the last 142 years. *Journal of Climate*, *30*(16), 6371–6389. https://doi.org/10.1175/JCLI-D-16-0646.1

Cerrone, D., Fusco, G., Simmonds, I., Aulicino, G., & Budillon, G. (2017). Dominant covarying climate signals in the Southern Ocean and Antarctic Sea ice influence during the last three decades. *Journal of Climate*, *30*(8), 3055–3072. https://doi.org/10.1175/JCLI-D-16-0439.1

Corrado, R., Lacorata, G., Palatella, L., Santoleri, R., & Zambianchi, E. (2017). General characteristics of relative dispersion in the ocean. *Scientific Reports*, *7*(1), 46291. https://doi.org/10.1038/srep46291

Cotroneo, Y., Budillon, G., Aliani, S., Capello, M., Ferrara, C., Paschini, E. & Spezie, G. (2018). Water temperature from XBT taken from the research vessel Italica in the Southern Ocean and Southwest Pacific Ocean from 2005-01-01 to 2005-01-06 (NCEI Accession 0173533), NOAA National Centers for Environmental Information. https://doi.org/10.7289/v5vh5m45

Cotroneo, Y., Budillon, G., Aliani, S., Ferrara, C., Greco, A., Meloni, R. & Spezie, G. (2018). Water temperature from XBT taken from the research vessel Italica in the Southern Ocean and Southwest Pacific Ocean from 2008-01-16 to 2008-01-21 (NCEI Accession 0174711), Version 1.1. NOAA National Centers for Environmental Information. https://doi.org/10.25921/Q29V-C980

Cotroneo, Y., Budillon, G., Artegiani, A., Conversano, F., Corbo, C., Gallarato, A., et al. (2018a). Water temperature data from XBT taken from the research vessel Italica in the Southern Ocean and Southwest Pacific Ocean from 1995-01-06 to 1995-03-02 (NCEI Accession 0170765), NOAA National Centers for Environmental Information. https://doi.org/10.7289/v53r0r5z

Cotroneo, Y., Budillon, G., Artegiani, A., Conversano, F., Corbo, C., Gallarato, A., et al. (2018b). Water temperature data from XBT taken from the research vessel Italica in the Southern Ocean and Southwest Pacific Ocean from 1994-11-03 to 1995-01-01 (NCEI Accession 0170608), NOAA National Centers for Environmental Information. https://doi.org/10.7289/v5rf5s9v

Cotroneo, Y., Budillon, G., Artegiani, A., Ferrara, C., Meloni, R., & Spezie, G. (2018). Water temperature from XBT taken from research vessel Italica in the Southern Ocean and Southwest Pacific Ocean from 1996-01-07 to 1996-02-18 (NCEI Accession 0171481), NOAA National Centers for Environmental Information. https://doi.org/10.7289/v5x065b9

Cotroneo, Y., Budillon, G., Bergamasco, A., Capello, M., De Stefano, M., Ferrara, C., et al. (2018). Water temperature data from XBT collected from research vessel Italica in Southern Ocean and Southwest Pacific Ocean from 1997-11-23 to 1998-03-06 (NCEI Accession 0172859). NOAA National Centers for Environmental Information. https://doi.org/10.7289/v50863mf

Cotroneo, Y., Budillon, G., Bergamasco, A., De Alteris, A., De Stefano, M., Ferrara, C., et al. (2018). Water temperature from XBT taken from the research vessel Italica in the Southern Ocean and Southwest Pacific Ocean from 2003-01-06 to 2003-01-11 (NCEI Accession 0173338), NOAA National Centers for Environmental Information. https://doi.org/10.7289/v5qz289c

Cotroneo, Y., Budillon, G., Bergamasco, A., De Stefano, M., Ferrara, C., Paschini, E., & Spezie, G. (2018). Water temperature from XBT taken from the research vessel Italica in the Southern Ocean and Southwest Pacific Ocean from 2001-01-06 to 2001-02-26 (NCEI Accession 0173213), NOAA National Centers for Environmental Information. https://doi.org/10.7289/v5s75dpg

Cotroneo, Y., Budillon, G., Castagno, P., Colizza, E., Cotterle, D., Falco, P., et al. (2018). Water temperature from XBT taken from the research vessel Araon in the Southern Ocean and Southwest Pacific Ocean from 2013-01-24 to 2013-02-06 (NCEI Accession 0174794). Version 1.1, NOAA National Centers for Environmental Information. https://doi.org/10.25921/9yts-p771

Cotroneo, Y., Budillon, G., Castagno, P., De Alteris, A., De Stefano, M., Falco, P., et al. (2017). Water temperature from XBT taken from research vessel Italica in the Southern Ocean and Southwest Pacific Ocean from 2012-01-13 to 2012-01-19 (NCEI Accession 0167834). NOAA National Centers for Environmental Information. https://doi.org/10.7289/v54j0cbw

Cotroneo, Y., Budillon, G., Conversano, F., Ferrara, C., & Spezie, G. (2018). Water temperature from XBT taken from the research vessel Italica in the Southern Ocean and Southwest Pacific Ocean from 1997-01-26 to 1997-02-19 (NCEI Accession 0172042), NOAA National Centers for Environmental Information. https://doi.org/10.7289/v5kd1w6b

Cotroneo, Y., Budillon, G., Ferrara, C., Meloni, R., Paschini, E., & Spezie, G. (2018). Water temperature from XBT taken from the research vessel Italica in the Southern Ocean and Southwest Pacific Ocean from 1999-01-05 to 1999-01-11 (NCEI Accession 0173211), NOAA National Centers for Environmental Information. https://doi.org/10.7289/v5mg7mtc

Cotroneo, Y., Budillon, G., Ferrara, C., Meloni, R., & Spezie, G. (2018). Water temperature from XBT taken from the research vessel Italica in the Southern Ocean and Southwest Pacific Ocean from 2007-02-05 to 2007-02-10 (NCEI Accession 0174709). Version 1.1, NOAA National Centers for Environmental Information. https://doi.org/10.25921/c8bm-xh74

Cotroneo, Y., Budillon, G., Ferrara, C., Monteduro, R., Russo, A., & Spezie, G. (2018). Water temperature from XBT taken from the research vessel Italica in the Southern Ocean and Southwest Pacific Ocean from 2003-12-24 to 2003-12-28 (NCEI Accession 0173328), NOAA National Centers for Environmental Information. https://doi.org/10.7289/v5vq3113

Cotroneo, Y., Budillon, G., Ferrara, C., Orsi, M., Paschini, E., Rivaro, P., & Spezie, G. (2018). Water temperature from XBT taken from the research vessel Italica in the Southern Ocean and Southwest Pacific Ocean from 2001-12-24 to 2001-12-31 (NCEI Accession 0173214), NOAA National Centers for Environmental Information. https://doi.org/10.7289/v5ng4nzr

Cotroneo, Y., Budillon, G., Ferrara, C., Paschini, E., Russo, A., & Spezie, G. (2018). Water temperature from XBT taken from the research vessel Italica in the Southern Ocean and Southwest Pacific Ocean from 2000-01-07 to 2000-02-18 (NCEI Accession 0173212), NOAA National Centers for Environmental Information. https://doi.org/10.7289/v56d5r8p

Cotroneo, Y., Budillon, G., Fusco, G., & Spezie, G. (2013). Cold core eddies and fronts of the Antarctic circumpolar current south of New Zealand from in situ and satellite data. *Journal of Geophysical Research: Oceans*, *118*, 2653–2666. https://doi.org/10.1002/jgrc.20193

Cotroneo, Y., Budillon, G., Meloni, R., Aliani, S., Zambardino, G., & Spezie, G. (2017). Water temperature data from XBT taken from research vessel Italica in the Southern Ocean and Southwest Pacific Ocean from 2010-01-25 to 2010-01-29 (NCEI Accession 0167835), NOAA National Centers for Environmental Information. https://doi.org/10.7289/v50r9mmm, *2017*.

Dee, D. P., Uppala, S., Simmons, A., Berrisford, P., Poli, P., Kobayashi, S., et al. (2011). The ERA-Interim reanalysis: Configuration and performance of the data assimilation system. *Quarterly Journal of the Royal Meteorological Society*, *137*(656), 553–597. https://doi.org/10.1002/qj.828

Falco, P., & Zambianchi, E. (2011). Near-surface structure of the Antarctic Circumpolar Current derived from World Ocean Circulation Experiment drifter data. *Journal of Geophysical Research*, *116*, C05003. https://doi.org/10.1029/2010JC006349

Fogt, R. L., & Bromwich, D. F. (2006). Decadal variability of the ENSO teleconnection to the high latitude South Pacific governed by coupling with the Southern Annual Mode. *Journal of Climate*, *19*(6), 979–997. https://doi.org/10.1175/JCLI3671.1

Fogt, R. L., Bromwich, D. F., & Hines, K. M. (2011). Understanding the SAM influence on the South Pacific ENSO teleconnection. *Climate Dynamics*, *36*(7–8), 1555–1576. https://doi.org/10.1007/s00382-010-0905-0

Foppert, A., Donohue, K. A., Randolph Watts, D., & Tracey, K. L. (2017). Eddy heat flux across the Antarctic circumpolar current estimated from sea surface height standard deviation. *Journal of Geophysical Research: Oceans*, *122*, 6947–6964. https://doi.org/10.1002/2017JC012837

Fusco, G., Cotroneo, Y., & Aulicino, G. (2018). Different behaviours of the Ross and Weddell seas surface heat fluxes in the period 1972–2015. *Climate*, *6*, 17. https://doi.org/10.3390/cli6010017

Gille, S. T. (2003). Float observations of the Southern Ocean. Part I: Estimating mean fields, bottom velocities, and topographic steering. *Journal of Physical Oceanography*, *33*(6), 1167–1181. https://doi.org/10.1175/1520-0485(2003)033<1167:footso>2.0.co;2

Grodsky, S. A., Lumpkin, R., & Carton, J. A. (2011). Spurious trends in global surface drifter currents. *Geophysical Research Letters*, *38*, L10606. https://doi.org/10.1029/2011GL047393

Hande, L. B., Siems, S. T., & Marton, M. (2012). Observed trends in wind speed over the Southern Ocean. *Geophysical Research Letters*, *39*, L11802. https://doi.org/10.1029/2012GL051734

Hogg, A. M., Meredith, M. P., Blundell, J. R., & Wilson, C. (2008). Eddy heat flux in the Southern Ocean: Response to variable wind forcing. *Journal of Climate*, *21*, 608–620. https://doi.org/10.1175/2007JCLI1925.1

Hogg, A. M., Meredith, M. P., Chambers, D. P., Abrahamsen, E. P., Hughes, C. W., & Morrison, A. K. (2015). Recent trends in the Southern Ocean eddy field. *Journal of Geophysical Research: Oceans*, *120*, 257–267. https://doi.org/10.1002/2014JC010470

Hughes, C. W., Meredith, M. P., & Heywood, K. J. (1999). Wind-driven transport fluctuations through Drake Passage: A southern mode. *Journal of Physical Oceanography*, *29*(8), 1971–1992. https://doi.org/10.1175/1520-0485(1999)029<1971:WDTFTD>2.0.CO;2

Jayne, S. R., & Marotzke, J. (2002). The oceanic eddy heat transport. *Journal of Physical Oceanography*, *32*, 3328–3345.

Jochum, M., & Eden, C. (2015). The connection between Southern Ocean winds, the Atlantic meridional overturning circulation, and indo-Pacific upwelling. *Journal of Climate*, *28*(23), 9250–9257. https://doi.org/10.1175/JCLI-D-15-0263.1

Langlais, C. E., Rintoul, S. R., & Zika, J. D. (2015). Sensitivity of Antarctic circumpolar current transport and eddy activity to wind patterns in the Southern Ocean. *Journal of Physical Oceanography*, *45*(4), 1051–1067. https://doi.org/10.1175/JPO-D-14-0053.s1

Legeais, J. F., Speich, S., Arhan, M., Ansorge, I. J., Fahrbach, E., Garzoli, S., & Klepikov, A. (2005). The baroclinic transport of the Antarctic Circumpolar Current south of Africa. *Geophysical Research Letters*, *32*, L24602. https://doi.org/10.1029/2005GL023271

Lin, X., Zhai, X., Wang, Z., & Munday, D. R. (2018). Mean, variability and trend of Southern Ocean wind stress: Role of wind fluctuations. *Journal of Climate*, *31*(9), 3557–3573. https://doi.org/10.1175/JCLI-D-17-0481.1

Mangoni, O., Saggiomo, V., Bolinesi, F., Margiotta, F., Budillon, G., Cotroneo, Y., et al. (2017). Phytoplankton blooms during austral summer in the Ross Sea, Antarctica: Driving factors and trophic implications. *PLoS ONE*, *12*(4), e0176033. https://doi.org/10.1371/journal.pone.0176033

Marshall, G. (2003). Trends in the southern annual mode from observations and reanalysis. *Journal of Climate*, *16*(24), 4134–4143. https://doi.org/10.1175/1520-0442(2003)

Marshall, J., & Shutts, G. (1981). A note on rotational and divergent eddy fluxes. *Journal of Physical Oceanography*, *11*, 1677–1680.

Menna, M., Poulain, P.-M., Bussani, A., & Gerin, R. (2018). Detecting the drogue presence of SVP drifters from wind slippage in the Mediterranean Sea. *Measurement*, *125*, 447–453. https://doi.org/10.1016/j.measurement.2018.05.022

Menna, M., Reyes Suarez, N. C., Civitarese, G., Gacic, M., Poulain, P.-M., & Rubino, A. (2019). Decadal variations of circulation in the Central Mediterranean and its interactions with the mesoscale gyres. *Deep Sea Research Oceans II*, *164*, 12–24. https://doi.org/10.1016/j.dsr2.2019.02.004

Meredith, M. P., & Hogg, A. M. (2006). Circumpolar response of Southern Ocean eddy activity to a change in the Southern Annual Mode. *Geophysical Research Letters*, *33*, L16608. https://doi.org/10.1029/2006GL026499

Meredith, M. P., Woodworth, P. L., Chereskin, T. K., Marshall, D. P., Allison, L. C., Bigg, G. R., et al. (2011). Sustained monitoring of the Southern Ocean at Drake Passage: Past achievements and future priorities. *Reviews of Geophysics*, *49*, RG4005. https://doi.org/10.1029/2010RG000348

Misic, C., Covazzi Harriague, A., Mangoni, O., Cotroneo, Y., Aulicino, G., & Castagno, P. (2017). Different responses of the trophic features of particulate organic matter to summer constraints in the Ross Sea. *Journal of Marine Systems*, *166*, 132–143. https://doi.org/10.1016/j.jmarsys.2016.06.012

Morrow, R., Marshall, L. W., Hogg, A. M., & Pasquet, S. (2010). Eddy response to the Southern Ocean climate modes. *Journal of Geophysical Research*, *115*, C10030. https://doi.org/10.1029/2009JC005894

Naveira Garabato, A. C., Ferrari, R., & Polzin, K. L. (2011). Eddy stirring in the Southern Ocean. *Journal of Geophysical Research*, *116*, C09019. https://doi.org/10.1029/2010JC006818

Orsi, A. H., Whitworth, T. W. III, & Nowlin, W. D. Jr. (1995). On the meridional extent and fronts of the Antarctic Circumpolar Current. *Deep Sea Research Part I*, *42*(5), 641–673. https://doi.org/10.1016/0967-0637(95)00021-W

Patara, L., Böning, C. W., & Biastoch, A. (2016). Multi-decadal trends in Southern Ocean eddy activity in 1/12° ocean model simulations. *Geophysical Research Letters*, *43*, 4517–4523. https://doi.org/10.1002/2016GL069026

Phillips, H. E., & Rintoul, S. R. (2000). Eddy variability and energetics from direct current measurements in the Antarctic Circumpolar Current south of Australia. *Journal of Physical Oceanography*, *30*(12), 3050–3076. https://doi.org/10.1175/1520-0485(2000)030<3050:EVAEFD>2.0.CO;2

Poulain, P.-M., Menna, M., & Mauri, E. (2012). Surface geostrophic circulation of the Mediterranean Sea derived from drifter and satellite Altimeter Data. *Journal of Physical Oceanography*, *42*(6), 973–990. https://doi.org/10.1175/JPO-D-11-0159.1

Pujol, M.-I., & Larnicol, G. (2005). Mediterranean Sea eddy kinetic energy variability from 11 years of altimetric data. *Journal of Marine Systems*, *58*(3–4), 121–142. https://doi.org/10.1016/j.jmarsys.2005.07.005

Ralph, E. A., & Niiler, P. P. (1999). Wind-driven currents in the tropical Pacific. *Journal of Physical Oceanography*, *29*(9), 2121–2129. https://doi.org/10.1175/1520-0485

Rinaldi, E., Buongiorno Nardelli, B., Zambianchi, E., Santoleri, R., & Poulain, P.-M. (2010). Lagrangian and Eulerian observations in the Tyrrhenian Sea. *Journal of Geophysical Research*, *115*, C04024. https://doi.org/10.1029/2009JC005535

Rintoul, S. R. (2018). The global influence of localized dynamics in the Southern Ocean. *Nature*, *558*(7709), 209–218. https://doi.org/10.1038/s41586-018-0182-3

Rintoul, S. R., Chown, S. L., DeConto, R. M., England, M. H., Fricker, H. A., Masson-Delmotte, V., et al. (2018). Choosing the future of Antarctica. *Nature*, *558*(7709), 233–241. https://doi.org/10.1038/s41586-018-0173-4

Rintoul, S. R., Hughes, C., & Olbers, D. (2001). The Antarctic circumpolar system. In G. Siedler, J. Church, J. Gould (Eds.), *Ocean circulation and climate*, *International Geophysics Series* (Vol. 77, pp. 271–302). London: Academic Press.

Rintoul, S. R., & Naviera Garabato, A. C. (2013). Dynamics of the Southern Ocean circulation. *Ocean Dynamics and Mixing*, *103*, 471–492. https://doi.org/10.1016/B978-0-12-391851-2.00018-0

Rintoul, S. R., Sokolov, S., & Church, J. (2002). A 6 year record of baroclinic transport variability of the Antarctic Circumpolar Current at 140°E from expendable bathythermograph and altimetry measurements. *Journal of Geophysical Research*, *107*(C10), 3155. https://doi.org/10.1029/2001JC000787

Rio, M. H. (2012). Use of altimeter and wind data to detect the anomalous loss of SVP-type drifter's drogue. *Journal of Atmospheric and Oceanic Tecnologies*, *29*(11), 1663–1674. https://doi.org/10.1175/JTECH-D-12-00008.1

Rivaro, P., Ardini, F., Grotti, M., Aulicino, G., Cotroneo, Y., Fusco, G., et al. (2018). Mesoscale variability related to iron speciation in a coastal Ross Sea area (Antarctica) during summer 2014. *Chemistry and Ecology*, *35*(1), 1–19. https://doi.org/10.1080/02757540.2018.1531987

Rivaro, P., Ianni, C., Langone, L., Ori, C., Aulicino, G., Cotroneo, Y., et al. (2017). Physical and biological forcing on the mesoscale variability of the carbonate system in the Ross Sea (Antarctica) during the summer season 2014. *Journal of Marine Systems*, *166*, 144–158. https://doi.org/10.1016/j.jmarsys.2015.11.002

Rivaro, P., Ianni, C., Raimondi, L., Manno, C., Sandrini, S., Castagno, P., et al. (2019). Analysis of physical and biogeochemical control mechanisms on summertime surface carbonate system variability in the western Ross Sea (Antarctica) using in situ and satellite data. *Remote Sensing*, *11*(3), 238. https://doi.org/10.3390/rs11030238

Sallée, J. B., Speer, K., & Morrow, R. (2008). Southern Ocean fronts and their variability to climate modes. *Journal of Climate*, *21*(12), 3020–3039. https://doi.org/10.1175/2007JCLI1702.1

Seymour, R. J. (2008). Decadal changes in very large wave occurrence on the US Pacific coast. Proceedings of the 31st International Conference on Coastal Engineering, ASCE, 1, 584–594.

Sgubin, G., Pierini, S., & Dijkstra, H. A. (2014). Intrinsic variability of the Antarctic Circumpolar Current system: Low- and high-frequency fluctuations of the Argentine Basin flow. *Ocean Science*, *10*(2), 201–213. https://doi.org/10.5194/os-10-201-2014

Sheen, K. L., Naviera Garabato, A. C., Brearley, J. A., Meredith, M. P., Polzin, K. L., Smeed, D. A., et al. (2014). Eddy-induced variability in the Southern Ocean abyssal mixing on climatic timescale. *Nature Geoscience*, *7*(8), 577–582. https://doi.org/10.1038/ngeo2200

Silvano, A., Foppert, A., Rintoul, S. R., Holland, P. R., Tamura, T., Kimura, N., et al. (2020). Recovery of Antarctic bottom water formed in the Ross Sea driven by anomalous climate forcing. *Nature Geoscience*. https://doi.org/10.1038/s41561-020-00655-3

Sokolov, S., & Rintoul, S. R. (2009). Circulation structure and distribution of the Antarctic Circumpolar Current fronts: 2. Variability and relationship to sea surface height. *Journal of Geophysical Research*, *114*, C11019. https://doi.org/10.1029/2008JC005248

Sprintall, J. (2003). Seasonal to interannual upper-ocean variability in the Drake Passage. *Journal of Marine Research*, *61*(1), 27–57, https://doi.org/10.1357/002224003321586408

Straub, D. N. (1993). On the transport and angular momentum balance of channel models of the Antarctic Circumpolar Current. *Journal of Physical Oceanography*, *23*(4), 776–782. https://doi.org/10.1175/1520-0485(1993)023<0776:OTTAAM>2.0.CO;2

Sun, B., Liu, C., & Wang, F. (2019). Global meridional eddy heat transport inferred from Argo and altimetry observations. *Scientific Reports*, *9*, 1345. https://doi.org/10.1038/s41598-018-38069-2

Swart, S., Speich, S., Ansorge, I. J., Goni, G. J., Gladyshev, S., & Lutjeharms, J. R. E. (2008). Transport and variability of the Antarctic Circumpolar Current south of Africa. *Journal of Geophysical Research*, *113*, C09014. https://doi.org/10.1029/2007JC004223

Thompson, A. F., & Naveira Garabato, A. C. (2014). Equilibration of the Antarctic Circumpolar Current by standing meanders. *Journal of Physical Oceanography*, *44*(7), 1811–1828. https://doi.org/10.1175/JPO-D-13-0163.1

Trani, M., Falco, P., & Zambianchi, E. (2011). Near-surface eddy dynamics in the Southern Ocean. *Polar Research*, *30*(1), 11203. https://doi.org/10.3402/polar.v30i0.11203

Trani, M., Falco, P., Zambianchi, E., & Sallée, J.-B. (2014). Aspects of the Antarctic Circumpolar Current dynamics investigated with drifter data. *Progress in Oceanography*, *125*, 1–15. https://doi.org/10.1016/j.pocean.2014.05.001

Treguier, A. M. (2010). Response of the Southern Ocean to the southern annual mode: Interannual variability and multidecadal trend. *Journal of Physical Oceanography*, *40*(7), 1659–1668. https://doi.org/10.1175/2010JPO4364.1

Volkov, D. L., Fu, L. L., & Lee, T. (2010). Mechanism of the meridional heat transport in the Southern Ocean. *Ocean Dynamics*, *60*(4), 791–801. https://doi.org/10.1007/s10236-010-0288-0

Webb, D. J., & de Cuevas, B. A. (2007). On the fast response of the Southern Ocean to changes in the zonal wind. *Ocean Science*, *3*, 417–427. https://doi.org/10.5194/os-3-417-2007

Wilson, C., Chris, W. H., & Blundell, J. R. (2015). Forced and intrinsic variability in the response to increased wind stress of an idealized Southern Ocean. *Journal of Geophysical Research: Oceans*, *120*, 113–130. https://doi.org/10.1002/2014JC010315

Wolter, K. & Timlin, M. S. (1993). Monitoring ENSO in COADS with a seasonally adjusted principal component index. Proc. of the 17th Climate Diagnostics Workshop, Norman, OK, NOAA/NMC/CAC, NSSL, Oklahoma Clim. Survey, CIMMS and the School of Meteor., Univ. of Oklahoma, 52–57, Conference proceeding.

Wolter, K., & Timlin, M. S. (1998). Measuring the strength of ENSO events—How does 1997/98 rank? *Weather*, *53*(9), 315–324. https://doi.org/10.1002/j.1477-8696.1998.tb06408.x

Wolter, K., & Timlin, M. S. (2011). El Niño/Southern Oscillation behaviour since 1871 as diagnosed in an extended multivariate ENSO index (MEI.ext). *International Journal of Climatology*, *31*(7), 1074–1087. https://doi.org/10.1002/joc.2336

Wunsch, C., & Stammer, D. (1995). The global frequency-wavenumber spectrum of oceanic variability estimated from TOPEX/POSEIDON altimeter measurements. *Journal of Geophysical Research*, *100*, 24,895–24,910.

Yelland, M., & Taylor, P. K. (1996). Wind-stress measurements from the open ocean. *Journal of Physical Oceanography*, *26*(4), 541–558. https://doi.org/10.1175/1520-0485(1996)026<0541:WSMFTO>2.0.CO;2